Rovibrational jet-cooled spectroscopy of the Kr–H2O van der Waals complex in the $\nu 2$ bending mode region of H2O

Y. Belkhodja, L. H. Coudert, P. Asselin

Rovibrational jet-cooled spectroscopy of the Kr−H_2O van der Waals complex in the ν_2 bending mode region of H_2O

Y. Belkhodja[a], L. H. Coudert[b,*], P. Asselin[a]

[a] *Sorbonne Université, CNRS, MONARIS, UMR 8233, 4 place Jussieu, Paris, F-75005, France*

[b] *Université Paris-Saclay, CNRS, Institut des Sciences Moléculaires d'Orsay, 91405, Orsay, France*

Abstract

Five rovibrational bands of the Kr−H_2O complex have been recorded in the ν_2 bending region of H_2O using a quantum cascade laser coupled to a pulsed slit supersonic jet. Four of them have been unambiguously assigned to the Σ and Π states in $v_2 = 1$, 1_{11}, 1_{10}, and 2_{12} rotational levels of the monomer based on ground state combination differences and similarities with the vibration-rotation tunneling states of Ar−H_2O. One of the bands is tentatively assigned to a combination band with two quanta of intermolecular van der Waals stretching mode (ν_s). Due to the efficient rovibrational cooling in our pulsed supersonic expansion, all observed bands originate from the lowest lying states. Four of them are from the lowest *ortho* ground state $\Sigma_e(1_{01})$ and one of them is from the lowest *para* ground state $\Sigma_e(0_{00})$. The jet-cooled spectra have been analyzed in terms of a nearly free internal rotor model taking into account Coriolis couplings between close lying Σ and

*Corresponding author: laurent.coudert@universite-paris-saclay.fr

Π levels. Molecular parameters for the five upper vibrational states, band origin, rotational and centrifugal distortion constants have been accurately determined. The β parameter describing the Coriolis coupling between the Σ and Π states originating from the (2_{12}) state has also been obtained.
Keywords: Kr−H_2O; weakly bond species; cold species; Quantum cascade laser; Coriolis coupling

1. Introduction

The accurate modeling of intermolecular interactions between water and rare gas (Rg) atoms has attracted particular attention for more than three decades. Rg−H_2O binary complexes are simple model systems for the study of hydrophobic and hydrogen bonding effects in aqueous solutions of chemical and biological systems and are an important step toward the thorough understanding of more complicated interactions between water and biological molecules. Molecular level understanding of the hydration of Rg atoms requires detailed knowledge about the geometry and intermolecular dynamics of these weakly bound complexes. The multidimensional intermolecular potential energy surface (IPES) of the floppy Rg−H_2O complexes generally displays shallow minima and low barriers and consequently large amplitude motions allowing them to sample regions of their IPES far from the minimum.

Numerous high resolution spectroscopic studies have been reported for Ar−H_2O in the microwave [1–3], (sub) millimeter-wave [4–8], and infrared (IR) spectral ranges [9–14]. The vibrational ground state of Ar−H_2O was characterized by Fraser *et al.* [1]. Vibration-rotation tunneling (VRT) states of Ar−H_2O studied using far-IR spectroscopy by Cohen *et al.* [4, 5, 7], Suzuki

et al. [6], and Zwart and Meerts [2] highlighted the strong Coriolis couplings mixing the internal rotation states of different symmetry and the need to introduce high order angular-radial couplings terms in the IPES. More recently, the high resolution infrared spectrum of Ar−H_2O was measured in both stretching and bending mode regions of H_2O by Nesbitt and coworkers [9–11] while Ar−D_2O was investigated in both bending mode [15, 16] and overtone [17] regions of D_2O.

The first IPES derived for Ar−H_2O is the AW2 empirical potential retrieved by Cohen *et al.* [7, 18, 19] and Hutson [20] fitting available experimental data of the complex. Other IPES were later computed [21–25] using *ab initio* calculations. In the most recent one, highly accurate analytical IPES of the full series of Rg−H_2O complexes were obtained by Makarewicz [25] at the CCSD(T)/CBS level of theory. For Ar−H_2O, a well depth quite close to that obtained from the AW2 empirical potential [7, 18–20] was found. For complexes with more polarizable atoms, it is expected that the H_2O molecule adopts a more hydrogen bonded position, consistent with a more anisotropic potential in the angular coordinate and a more hindered internal rotation in Kr−H_2O and Xe−H_2O complexes than in Ar−H_2O [26]. For these three species, Table 1 compares calculated energy and pseudodiatomic distance for the global minimum of their potential energy surface. Both quantities increase when going to heavier species.

Fewer results are available for complexes with a Rg atom other than argon. Rotational spectra of various isotopomers of Kr−H_2O [27] and Xe−H_2O [28] were measured by Jäger and coworkers providing us with reliable rotational constants and nuclear quadrupole coupling. A 3-D *ab initio* IPES of Xe−H_2O

was built at the CCSD(T) level to provide information about the H_2O angular motions and molecular structure complemented by spectroscopic results. In the near-infrared range, Vanfleteren *et al.* [29, 30] investigated the intermolecular dynamics of Kr−H_2O in the combination and overtone OH stretching mode region of H_2O but no infrared studies were reported in the fundamental modes regions. This justifies a reliable spectroscopic investigation of Rg−H_2O complexes, with Rg atoms other than argon, in these regions.

The present study reports the first spectroscopic investigation of the Kr−H_2O complex in the ν_2 bending mode region of water. Quantum cascade laser spectroscopy coupled to a pulsed slit supersonic jet was used. Five bands could be observed near 1618, 1634, 1653, 1658, and 1663 cm^{-1} and, making use of the similarities between the Ar−H_2O and Kr−H_2O energy level diagrams, were assigned on the grounds of the bands identified for Ar−H_2O in the the ν_2 bending mode region by Weida and Nesbitt [11], and Liu and Xu [13]. Rovibrational analyses of the only *ortho*-Kr−H_2O and the four *para*-Kr−H_2O bands allowed us to derive accurate vibrational energy levels and rovibrational parameters for the rotor internal states which could serve to build an advanced four dimensional IPES taking into account explicitly the ν_2 bending mode and to evaluate the effects of Rg atom (Rg=Ar, Kr) on Coriolis couplings.

2. Experimental

The rovibrational spectra of Kr−H_2O have been recorded in the 1615–1665 cm^{-1} region of the ν_2 bending mode of H_2O using the SPIRALES set-

Table 1: Global minimum energy and pseudodiatomic distance[a] for the potential energy surface of several Rg−H_2O complexes

Complex	Reference	Energy (cm^{-1})	R (Å)	Method
Ar−H_2O	Ref. [19]	−143.0	3.636	Exp. data
	Ref. [24]	−142.7	3.651	*Ab initio*
	Ref. [25]	−140.9	3.695	*Ab initio*
Kr−H_2O	Ref. [25]	−167.9	3.845	*Ab initio*
Xe−H_2O	Ref. [25]	−191.7	4.03	*Ab initio*

[a] Energies and pseudodiatomic distances are reported in the columns headed Energy and R, respectively.

up, a jet-cooled laser spectrometer which couples an external-cavity quantum cascade laser (EC-QCL) and a pulsed free supersonic jet to probe by direct absorption the molecular complexes cooled down in the adiabatic expansion. The SPIRALES set-up has already been described in detail in recent papers [31, 32] and only the main characteristics and most recent developments will be presented hereafter.

The light source is a continuous-wave room-temperature mode hop-free EC-QCL with a spectral width of about 10 MHz, which spans the 1615–1690 cm^{-1} range (Daylight Solutions). Less than 10% of the total light is sent through two channels. The first one, for relative frequency calibration, is a solid germanium etalon with a free spectral range of 490 MHz [32]. A 15 cm length reference cell containing a known reference gas at a pressure of about 5 mbar (NH_3 and H_2O in the present work) is used in the second

channel for absolute frequencies calibration. The accuracy for line positions thus achieved is 0.0005 cm^1. The remaining part of the light is sent through a multipass optical cavity mounted in the jet chamber and composed of two 1.5″ astigmatic mirrors ($R = 99.2\%$, AMAC-36, Aerodyne Research) aligned according to a 182-pass configuration.

The molecular jet is produced from a pulsed nozzle (General Valve Series 9) by fitting a 0.9 mm diameter pin hole nozzle with two modified industrial blades, forming a 30 mm length $\times$ 150 μm width slit opening, and serving as the molecular expansion source. Recent implementation of a six-way distribution gas channel already used by the Calgary group [33] ensures a homogeneous distribution of the gas along the slit which limits Doppler line broadening and still increases the absorption path. Experimental full-width-at-half-maximum (FWHM) line widths of rovibrational lines measured in the present work reach typically 50 MHz.

Supersonic expansion conditions have been optimized to get the highest absorption signal, in particular dilution and total backing pressure P_0 of the binary rare gas mixture Kr/Ne sweeping above the water vapor flow at ambient temperature. The Kr$-$$H_2O$ spectra presented hereafter were recorded with Kr/Ne = 1/7 and P_0 equal to 12 bar. Van der Waals complexes were probed by the infrared laser light at axial distances in the 2–12 mm range from the nozzle exit to keep a sufficient density to be probed in the slit jet expansion. Due to the presence of intense ν_2 bands of H_2O monomer in the vicinity of Kr$-$$H_2O$ bands, the path of the QCL source outside the experimental chamber is operated in a Plexiglas box filled with dry atmospheric N_2.

3. Results

Below, the VRT states of the complex are denoted $n_s, K(jk_ak_c)$, where n_s is the vibrational quantum number for the van der Waals stretching mode, K is the projection of the total rotational angular momentum **J** onto the Kr−H_2O pseudodiatomic axis, and jk_ak_c is a usual asymmetric top label describing the rotational level of the the almost freely rotating water molecule. Like in linear molecules, the labels Σ, Π, Δ are used for $K = 0, 1, 2$, respectively. VRT states can be characterized by their nuclear spin-modification which is *ortho* and *para* for a symmetric and antisymmetric nuclear spin function with statistical weights equal to 3 and 1, respectively. *Ortho* and *para* states correspond to $k_a + k_c$ odd and even, respectively. Rotational levels arising from the complex VRT states are identified with the rotational quantum number J and the symmetry labels e/f such that e and f levels have a parity $p = (-1)^J$ and $p = (-1)^{J+1}$, respectively. In principle, the vibrational quantum number ν_2 should also be used to identify the monomer states involved in the present investigation. It will be ignored most of the time since, for all five bands assigned in this work, we have $v_2 = 1$ and 0 for the upper and lower VRT states, respectively. When the vibrational quantum number for the van der Waals stretching mode is zero, it will also be omitted in the VRT state label.

3.1. Energy levels involved the ν_2 transition of Kr−H_2O

The spectra recorded in this work were assigned using the similarity between the VRT states of Ar−H_2O and those of Kr−H_2O in the ground and $v_2 = 1$ vibrational states of the H_2O monomer. Thanks to the pioneering far-

infrared studies of Cohen *et al.* [4, 5, 7], the lowest VRT states of Ar−H_2O in $v_2 = 0$ are spectroscopically well characterized. For *para* states, the transition $n_s = 1, \Sigma_e(0_{00}) \leftarrow \Sigma_e(0_{00})$ from the $\Sigma_e(0_{00})$ ground state to the first excited state of the van der Waals stretching fundamental at 30.244 cm^{-1} was observed. For *ortho* states, three transitions $n_s = 1, \Sigma_e(1_{01}) \leftarrow \Sigma_e(1_{01})$; $n_s = 1, \Sigma_e(1_{10}) \leftarrow \Pi(1_{01})$; and $\Pi(1_{10}) \leftarrow \Sigma_e(1_{01})$ were measured. The two latter transitions allowed Cohen *et al.* [4, 5, 7] to observe for the first time the $\Pi(1_{01})$ and $\Pi(1_{10})$ states. The VRT states of Ar−H_2O in the $v_2 = 1$ state are also well characterized thanks to the results of Weida and Nesbitt [11], and Liu and Xu [13].

Figure 1 displays the VRT states involved in the ν_2 observed transitions of both Ar−H_2O and Kr−H_2O. For the former, the results obtained previously [4, 5, 7, 11, 13] were used and for $v_2 = 0$ only low lying states are shown, namely, the lowest *para* state and the three *ortho* states, $\Pi(1_{10})$, $\Pi(1_{01})$, and $\Sigma_e(1_{01})$, where the two Π states are respectively 21.264 and 11.528 cm^{-1} above $\Sigma_e(1_{01})$. For Kr−H_2O, the states shown in Fig. 1 were derived from the present study. For $v_2 = 0$, only low lying states expected to be populated in a supersonic expansion are shown, i.e. the *para* $\Sigma_e(0_{00})$ state and the three *ortho* $\Sigma_e(1_{01})$, $\Pi(1_{01})$, and $\Pi(1_{10})$ states, roughly 10 cm^{-1} from each other. The five $v_2 = 1 \leftarrow 0$ transitions observed in this work include only one band for *para*-Kr−H_2O, the $\Pi(1_{11}) \leftarrow \Sigma_e(0_{00})$ and four bands for *ortho*-Kr−H_2O, the $\Pi(1_{10}) \leftarrow \Sigma_e(1_{01})$; $n_s = 2, \Sigma_e(1_{01}) \leftarrow \Sigma_e(1_{01})$; $\Sigma_e(2_{12}) \leftarrow \Sigma_e(1_{01})$; and $\Pi(2_{12}) \leftarrow \Sigma_e(1_{01})$, originating from the same state. The fact that for both *para*- and *ortho*-Kr−H_2O only the lowest states, $\Sigma_e(0_{00})$ and $\Sigma_e(1_{01})$, respectively, are observed is due to the very low temperature achieved with our

SPIRALES set-up. With the higher temperature of 18 K achieved with the CW-CRDS spectrometer of Herman's group [29, 30], transitions originating from $\Pi(1_{01})$ and $\Pi(1_{10})$ states could also be observed. Observed wavenumbers for the five transitions observed in this work are reported in Tables 2 and 3. From the analyses reported below and, more precisely, comparing observed and simulated spectra, the rotational temperature with the SPIRALES set-up was estimated to be about 6 K.

3.2. Jet-cooled laser results and rovibrational analysis

In the following, we present the rovibrational analysis of the five bands observed for $Kr-H_2O$ in the monomer ν_2 band. The energy levels of the internal rotor states are modeled using the standard linear-molecule-like rotational energy expression [1]:

$$E(J) = E_0 + BJ(J+1) - D[J(J+1)]^2 + H[J(J+1)]^3 \qquad (1)$$

where E_0, B, D, and H are the rotationless energy, the rotational constant, and the quartic and sextic centrifugal distortion constants, respectively. In the line position analysis, the selection rules for the e/f symmetry labels were taken into account. For P and R lines, we have $e \leftrightarrow e$ and $f \leftrightarrow f$; for Q lines, $f \leftrightarrow e$. Since for all five observed bands, the ground state levels have e symmetry, P and R lines allow us to access e symmetry levels while Q lines allow us to access f symmetry levels. In the near-infrared study reported in the H_2O first harmonic of the OH stretching mode region, successful rotational analyses of 7 *ortho* $^{84}Kr-H_2O$ transitions could be only performed including a Coriolis coupling between the $\Sigma_e(1_{01})$ and $\Pi(1_{01})$ *ortho* lower states [29]. This should also be considered in the present work. Several Coriolis or Fermi

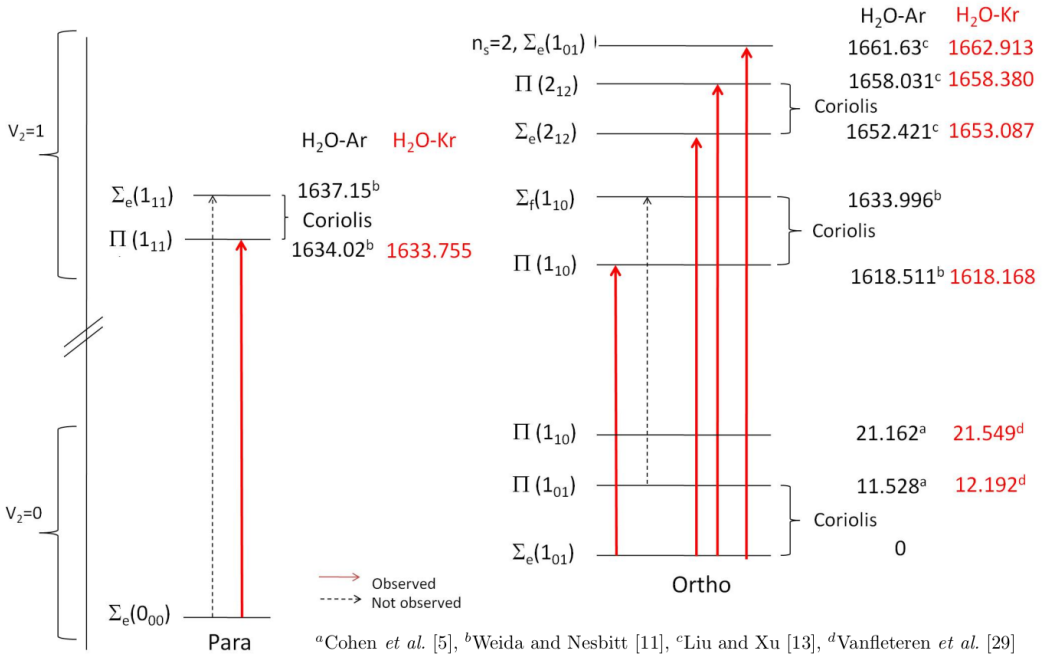

[a]Cohen *et al.* [5], [b]Weida and Nesbitt [11], [c]Liu and Xu [13], [d]Vanfleteren *et al.* [29]

Figure 1: Lowest internal rotor energy levels in the $v_2 = 0$ and 1 states of Kr−H_2O are compared to those of Ar−H_2O. VRT states are identified using the labeling scheme of Section 3. The vibrational quantum number for the van der Waals stretching mode n_s is omitted when zero. The five mid-infrared bands of Kr−H_2O observed in this work are indicated by thick lines. The two dashed lines indicate transitions observed in Ar−H_2O but not in Kr−H_2O, involving the $\Sigma_e(1_{11})$ and $\Sigma_f(1_{10})$ upper states coupled by Coriolis interactions with $\Pi(1_{11})$ and $\Pi(1_{10})$, respectively. The energies given for Kr−H_2O were determined in the analyses carried out in this work. The Coriolis couplings between Σ and Π states identified in both $v_2 = 0$ and 1 states of Ar−H_2O are indicated in this energy scheme.

Table 2: Observed minus calculated table for the transitions at 1618, 1633, and 1663 cm^{-1}

Trns[a]	Obs[b]	O−C[c]	Trns[a]	Obs[b]	O−C[c]	Trns[a]	Obs[b]	O−C[c]
				$\Pi(1_{10}) \leftarrow \Sigma_e(1_{01})$				
$P(11)$	1616.7905	−0.1	$R(1)$	1618.4960	0.0	$Q(1)$	1618.1712	0.0
$P(10)$	1616.8844	−0.7	$R(2)$	1618.6694	0.6	$Q(2)$	1618.1779	−0.1
$P(9)$	1616.9852	−0.6	$R(3)$	1618.8480	0.5	$Q(3)$	1618.1881	−0.1
$P(8)$	1617.0923	−0.5	$R(4)$	1619.0321	0.2	$Q(4)$	1618.2016	−0.2
$P(7)$	1617.2057	−0.3	$R(5)$	1619.2228	0.7	$Q(5)$	1618.2189	0.0
$P(6)$	1617.3250	−0.3	$R(6)$	1619.4180	−0.1	$Q(6)$	1618.2394	0.0
$P(5)$	1617.4505	−0.3	$R(7)$	1619.6205	0.6	$Q(7)$	1618.2634	0.0
$P(4)$	1617.5823	0.1	$R(8)$	1619.8278	0.4	$Q(8)$	1618.2910	0.1
$P(3)$	1617.7198	0.1	$R(9)$	1620.0413	0.6	$Q(9)$	1618.3220	0.0
$P(2)$	1617.8628	−0.4	$R(10)$	1620.2597	0.0	$Q(10)$	1618.3566	−0.1
$R(0)$	1618.3289	−0.1	$R(11)$	1620.4845	−0.1	$Q(11)$	1618.3950	0.0
				$\Pi(1_{11}) \leftarrow \Sigma_e(0_{00})$				
$P(2)$	1633.4317	−0.7	$Q(6)$	1633.7684	0.1	$R(4)$	1634.4535	0.0
$P(3)$	1633.2617	−0.4	$Q(7)$	1633.7720	−0.2	$R(5)$	1634.5735	−0.1
$P(4)$	1633.0857	0.1	$Q(8)$	1633.7762	−0.4	$R(6)$	1634.6867	0.0
$P(5)$	1632.9034	0.4	$Q(9)$	1633.7806	−0.5	$R(7)$	1634.7924	−0.1
$P(6)$	1632.7149	0.7	$Q(10)$	1633.7854	−0.3	$R(8)$	1634.8907	0.0
$P(7)$	1632.5193	0.2	$Q(11)$	1633.7909	0.5	$R(9)$	1634.9805	−0.5
$P(8)$	1632.3176	0.1	$R(0)$	1633.9071	−0.3	$R(10)$	1635.0632	0.2
$Q(3)$	1633.7598	0.7	$R(1)$	1634.0527	−0.7	$R(11)$	1635.1365	0.1
$Q(4)$	1633.7624	0.8	$R(2)$	1634.1929	−0.4			
$Q(5)$	1633.7653	0.6	$R(3)$	1634.3268	0.1			
				$n_s = 2, \Sigma(1_{01}) \leftarrow \Sigma_e(1_{01})$				
$R(1)$	1663.2110	0.7	$R(7)$	1664.0235	0.3	$P(6)$	1661.9212	−0.4
$R(2)$	1663.3527	−0.4	$P(1)$	1662.7580	0.7	$P(7)$	1661.7445	−0.8
$R(3)$	1663.4922	0.0	$P(2)$	1662.5976	−0.1	$P(8)$	1661.5673	−0.3
$R(4)$	1663.6277	−0.5	$P(3)$	1662.4338	−0.2	$P(9)$	1661.3888	−0.4
$R(5)$	1663.7606	−0.9	$P(4)$	1662.2665	0.0	$P(10)$	1661.2110	−0.1
$R(6)$	1663.8958	2.9	$P(5)$	1662.0953	−0.2	$P(11)$	1661.0343	−0.2

[a] Rotational assignments are given in this column.

[b] Observed wavenumbers are given in this column in cm^{-1}.

[c] Residuals are given in this column in 10^{-3} cm^{-1}.

Table 3: Observed minus calculated table for the transitions at 1653 and 1658 cm^{-1}

Trns[a]	Obs[b]	O−C[c]	O−C[d]	Trns[a]	Obs[b]	O−C[c]	O−C[d]
$\Sigma_e(2_{12}) \leftarrow \Sigma_e(1_{01})$							
$P(10)$	1656.9010	−1.0	−0.7	$R(10)$	1660.0809	0.8	0.3
$P(9)$	1657.0682	−0.4	−0.1	$R(11)$	1660.1698	0.2	−0.4
$P(8)$	1657.2230	−0.7	−0.6	$R(12)$	1660.2379	−0.3	0.1
$P(7)$	1657.3706	0.2	0.1	$Q(1)$	1658.3759	−0.8	−0.4
$P(6)$	1657.5117	0.1	−0.2	$Q(2)$	1658.3710	−0.4	−0.1
$P(5)$	1657.6501	−0.2	−0.5	$Q(3)$	1658.3629	−0.6	−0.4
$P(4)$	1657.7899	1.0	0.8	$Q(4)$	1658.3530	0.0	0.1
$P(3)$	1657.9301	0.4	0.4	$Q(5)$	1658.3400	0.0	0.0
$R(0)$	1658.5403	0.1	0.3	$Q(6)$	1658.3248	0.2	0.2
$R(1)$	1658.7058	−0.2	−0.2	$Q(7)$	1658.3069	0.1	0.1
$R(2)$	1658.8758	0.3	0.1	$Q(8)$	1658.2866	−0.1	−0.1
$R(3)$	1659.0468	−0.2	−0.5	$Q(9)$	1658.2645	0.3	0.2
$R(4)$	1659.2187	0.5	0.2	$Q(10)$	1658.2397	0.1	0.1
$R(5)$	1659.3869	0.4	0.3	$Q(11)$	1658.2126	0.0	0.0
$R(6)$	1659.5491	0.0	0.2	$Q(12)$	1658.1831	−0.3	−0.2
$R(7)$	1659.7028	0.1	0.4	$Q(13)$	1658.1519	0.0	0.2
$R(8)$	1659.8445	0.2	0.4	$Q(14)$	1658.1181	0.2	0.4
$R(9)$	1659.9711	0.1	0.1	$Q(15)$	1658.0812	−0.1	0.0
$\Pi(2_{12}) \leftarrow \Sigma_e(1_{01})$							
$P(12)$	1649.8944	0.8	0.8	$R(3)$	1653.4752	−0.6	−0.6
$P(11)$	1650.2451	−0.1	0.0	$R(4)$	1653.5188	−0.9	−0.8
$P(10)$	1650.5852	−0.1	−0.2	$R(5)$	1653.5448	−0.3	−0.3
$P(9)$	1650.9140	0.5	0.4	$R(6)$	1653.5538	−0.1	−0.1
$P(8)$	1651.2293	0.8	0.7	$R(7)$	1653.5475	−0.1	−0.1
$P(7)$	1651.5292	0.2	0.3	$R(8)$	1653.5276	−0.1	−0.1
$P(6)$	1651.8128	−0.3	−0.2	$R(9)$	1653.4949	−0.4	−0.3
$P(5)$	1652.0798	0.7	0.8	$R(10)$	1653.4502	−0.6	−0.6
$R(2)$	1653.4123	0.4	0.3				

[a] Rotational assignments are given in this column.

[b] Observed wavenumbers are given in this column in cm^{-1}.

[c] Residuals, in 10^{-3} cm^{-1}, from the separate analysis of both bands ignoring the Coriolis coupling.

[d] Residuals, in 10^{-3} cm^{-1}, from the simultaneous analysis of both bands taking into account the Coriolis coupling.

couplings are also expected in the $v_2 = 1$ state. For *para* transitions, the $\Pi(1_{11})$ state is perturbed by both $n_s = 1, \Sigma_e(0_{00})$ and $\Sigma_e(1_{11})$ states, located 8.5 cm^{-1} below and 3.1 cm^{-1} above, respectively, in Ar−H_2O [11]. For *ortho* transitions, a weak perturbation is expected between the observed $\Pi(1_{10})$ level and $\Sigma_f(1_{10})$, located 15.5 cm^{-1} above in Ar−H_2O [11]. At last, a strong Coriolis coupling is expected between the $\Sigma_e(2_{12})$ and $\Pi_e(2_{12})$ levels, 5.6 cm^{-1} apart in Ar−H_2O [11].

Two different approaches were used for the line position analysis: (A) if the perturbing levels are not observed, the transition is analyzed using Eq. (1). For Π levels, the Π_e and Π_f levels are treated using the same rotationless energy, but different rotational and distortion constants. The former being used for both P and R branches; the latter for the Q branch. (B) If the perturbing level is observed (as in the case of the $\Pi(2_{12})$ level), the rotational energy is computed digaonalizing a 2×2 matrix with a Coriolis coupling term. This matrix is given by:

$$\begin{pmatrix} H_{\text{rot}}^{\Sigma} & H_{\text{Cor}} \\ H_{\text{Cor}} & H_{\text{rot}}^{\Pi} \end{pmatrix} \tag{2}$$

where diagonal terms H_{rot}^{Σ} and H_{rot}^{Π} are unperturbed rotational energies for Σ and Π states calculated with Eq. (1) and H_{Cor}, the J-dependent Coriolis coupling between Σ and Π states, is given by $\beta\sqrt{J(J+1)}$, where β is the Coriolis coupling constant. All the simulations were performed with the PGOPHER [34, 35] software which allows us to evaluate rotational energies as calculated from Eqs. (1) and (2).

3.2.1. Para-*Kr*−H_2O *band*

A single *para*-Kr−H_2O band has been identified in the ν_2 bending mode region and assigned to the $\Pi(1_{11}) \leftarrow \Sigma_e(0_{00})$ transition by analogy with that observed by Weida and Nesbitt [11] at 1633.996 cm^{-1}. Figure 2(a) displays its full spectrum and emphasizes that its band center is only 0.2 cm^{-1} below that of Ar−H_2O. The band is characterized by an intense Q branch degraded to the higher frequency side and a marked asymmetry of P and R branches accessing e perturbed levels. The lower state assignment was checked using the microwave study of van Wijngaarden and Jäger [27] which provides us with ground state combination differences (GSCD). An excellent agreement is found between the energy difference of the $J = 4$ and 2 levels of the $v_2 = 0, \Sigma_e(0_{00})$ state and the wavenumber difference of the two rotational lines observed at 1634.1929 and 1633.0857 cm^{-1}, both difference being equal to 1.1072 cm^{-1}. The $\Sigma_e(1_{11})$ state, expected to be about 3 cm^{-1} above $\Pi(1_{11})$ (by analogy with Ar−H_2O) has not been observed, consequently this transition has been analyzed according to the case (A). The e perturbed and f unperturbed components of the $\Pi(1_{11})$ state are treated using the following set of spectroscopic constants: E_0, B_e, B_f, D_e, D_f. While the Coriolis coupling constant β cannot be derived from the rovibrational analysis, the relative magnitude of coupling effects can be estimated from the splitting of e and f levels as well as from the difference between the rotational constants B_e and B_f and that of the ground state B''. The PGOPHER simulated spectrum at a rotational temperature of 6 K was calculated with the spectroscopic constants just described. The resulting spectrum is displayed in Fig. 2(b). Table 4 lists the spectroscopic constants derived from the line

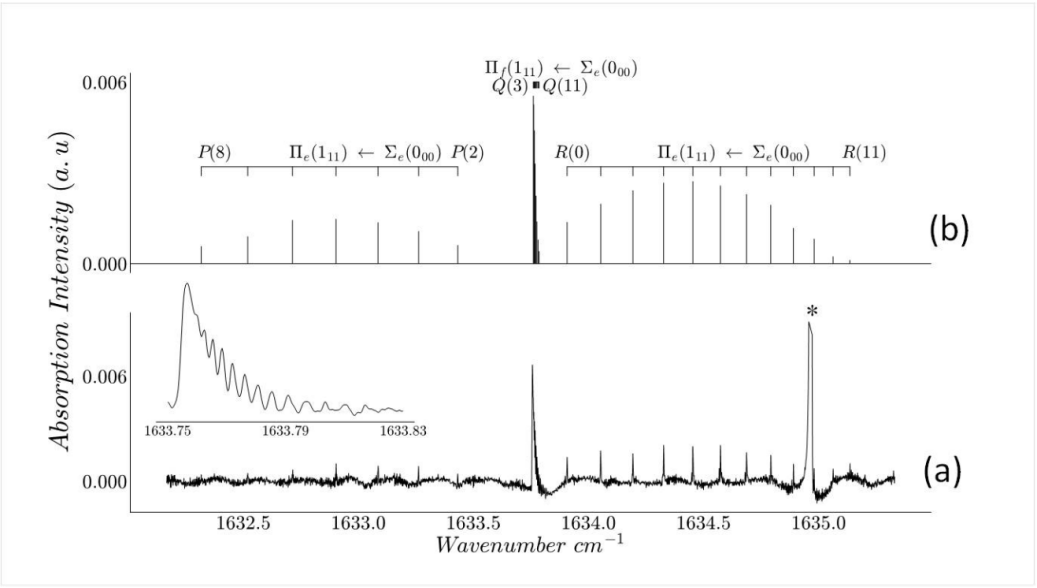

Figure 2: Jet-cooled laser spectrum of the $\Pi(1_{11}) \leftarrow \Sigma_e(0_{00})$ *para* transition of Kr−H_2O (a) compared to the PGOPHER fit of 28 lines using the spectroscopic parameters in Table 4. An expanded view of the partially resolved Q branch clearly emphasizes that it degrades towards high frequency which is consistent with the rotational constant in the excited state being larger than in the ground state. As discussed in Section 3.2.1, P and R branches were fitted separately from the Q branches due to the symmetry selection rules, $e \leftrightarrow e$ for the P and R branches and $f \leftrightarrow e$ for the Q branch. The intense line marked by an asterisk is the $1_{11} \leftarrow 0_{00}$ transition of H_2O monomer at 1634.967 cm^{-1}.

position analysis. In this table, the subband centers ν_0 stands for the energy difference $E_0 - E''$. The fact that B_e is 4.2% smaller than B_f gives rise to the P-R branches asymmetry and clearly confirms that the coupling state $\Sigma_e(1_{11})$ is above $\Pi(1_{11})$.

3.2.2. Ortho-$Kr{-}H_2O$ *bands*

Four *ortho* Kr$-$H$_2$O bands could be unambiguously identified on the grounds of band centers very close to those of Ar$-$H$_2$O and of GSCD consistent with the frequencies reported by van Wijngaarden and Jäger [27] for the $v_2 = 0, \Sigma_e(1_{01})$ state.

The band centered at 1618.2 cm^{-1}, displayed in Fig. 3a, is typical of the $\Pi \leftarrow \Sigma$ vibrational band of a linear molecule as confirmed by the presence of an $R(0)$ transition, a strong Q branch, and a missing $P(1)$ transition. Thanks to the high intensity of this band, the four main isotopic species of krypton can be observed in natural abundance, ^{82}Kr (11.3%), ^{83}Kr (11.5%), ^{84}Kr (57.0%), and ^{86}Kr (17.3%), in the $P(J)$ and $R(J)$ line structure. The inset for the $R(6)$ line in Fig. 3a shows that this line is split into four components with decreasing line positions for increasing krypton mass. An accurate linear dependence of the line position with the mass can be observed. Below, the rovibrational analysis results are given for the main ^{84}Kr isotopic species since the best S/N ratio is obtained for this species. For the other bands observed in this investigation, the less favorable S/N ratio only allowed us to observe this main isotopic species, even in the case of the $\Sigma_e(2_{12}) \leftarrow \Sigma_e(1_{01})$ band which, as emphasized by Fig. 5, displays a fairly favorable S/N ratio.

This band is assigned to the *ortho* $\Pi(1_{10}) \leftarrow \Sigma_e(1_{01})$ transition by analogy with that observed at 1618.511 cm^{-1} by Weida and Nesbitt [11]. The $\Sigma_f(1_{10})$ state, expected to be about 15 cm^{-1} above $\Pi(1_{10})$ according to these authors, has not been observed. Consequently this transition has been analyzed in the same way as the *para* $\Pi(1_{11}) \leftarrow \Sigma_e(0_{00})$ transition. Figure 3b displays the spectrum simulated with the spectroscopic parameters thus obtained. This

time, a B_f value 1.6% smaller then B_e clearly confirms the presence of a weakly coupled state $\Sigma_f(1_{10})$ above $\Pi(1_{10})$.

The weak band displayed in Fig. 4a in the 1661–1664 cm^{-1} range is more difficult to assign. An Ar−H_2O band displaying a similar pattern has been observed in the same region [13, 36] and tentatively assigned to the *para* $n_s = 1, \Sigma_e(1_{11}) \leftarrow \Sigma_e(0_{00})$ band. An unsatisfactory analysis could only be achieved using different B_e, D_e, and H_e spectroscopic constants for the P and R branches [36]. The negative fitted values obtained with the R branch for D_e and H_e may be due to perturbation from other internal rotor states. The assignment proposed in Refs. [13, 36] is not appropriate for the band observed in this work because it does not seem to be perturbed and GSCD clearly show that there is a match between the energy difference of the $J = 4$ and 2 levels of the $v_2 = 0, \Sigma_e(1_{01})$ state and the wavenumber difference of the lines observed at 1663.3527 and 1662.2665 cm^{-1}, both differences being equal to 1.0866 cm^{-1}. A $\Sigma \leftarrow \Sigma$ transition being expected in the absence of Q branch, the most likely candidate is $n_s = 2, \Sigma_e(1_{01}) \leftarrow \Sigma_e(1_{01})$. This choice relies on the energy level diagram of $j = 1$ VRT states in $v_2 = 0$ calculated from the AW1 empirical potential of Ar−H_2O [7]. The ν_s stretching frequency for the $v_2 = 0, \Sigma_e(1_{01})$ level being 33.9 cm^{-1} in Ar−H_2O [7], the $n_s = 2, \Sigma_e(1_{01}) \leftarrow \Sigma_e(1_{01})$ transition is calculated at 1661.63 cm^{-1} which is quite close to the observed band center of 1662.913 cm^{-1}. Fig. 4b displays the simulated spectrum based on the values of the E_0, B_e, D_e spectroscopic parameters describing the $n_s = 2, \Sigma_e(1_{01})$ state.

Last, the bands observed in the 1649.8–1653.6 and 1656.9–1660.3 cm^{-1} ranges were assigned to the $\Sigma_e(2_{12}) \leftarrow \Sigma_e(1_{01})$ and $\Pi(2_{12}) \leftarrow \Sigma_e(1_{01})$ tran-

sitions (Figs. 5a and 6a), respectively, by analogy with those observed by Liu and Xu [13] in the Ar−H_2O complex. A strong Coriolis coupling was identified between the $\Sigma_e(2_{12})$ and $\Pi(2_{12})$ states. To analyze these coupled bands, we first carried out separate fits of both bands according to case (A). For the Π state seven parameters were used, E_0, B_e, B_f, D_e, D_f, H_e, H_f, including the sextic parameters H_e and H_f to compensate for coupling effects in the upper states. Our best fit yields the stick spectrum in Fig. 6b. The large variations observed at high J-values between successive $P(J)$ and $R(J)$ lines suggests that the Coriolis perturbation takes place between states of e symmetry. The spectroscopic parameters values in Table 4 provide us with qualitative information about the strength of this Coriolis coupling. A 5.4% increase of B_e relative to B'' is consistent with a close lying $\Sigma_e(2_{12})$ state, 5.3 cm^{-1} lower than $\Pi_e(2_{12})$. The large value of H_e for this state, about 40 times larger than for the unperturbed $\Pi_f(2_{12})$ state, confirms the strong effect of the coupling. The R branch turning point observed for the $\Sigma_e(2_{12}) \leftarrow \Sigma_e(1_{01})$ transition (Fig. 5a) is as for Ar−H_2O indicative [13] of a strong coupling. At last, for the $\Sigma_e(2_{12})$ state, a negative and unusually large value of D_e compared to that of $\Pi_e(1_{10})$ is also due to the large magnitude of the coupling. The root-mean-square (RMS) deviation of the fit involving the $\Sigma_e(2_{12})/\Pi(2_{12})$ pair of states being twice larger than for the weakly coupled $\Pi_e(1_{10})$ state emphasizes that separate analyses are not appropriate for these strongly coupled states.

Contrary to the other transitions presented in this study, in the $\Sigma_e(2_{12}) \leftarrow \Sigma_e(1_{01})$ and $\Pi(2_{12}) \leftarrow \Sigma_e(1_{01})$ transitions, the Coriolis coupling could be accurately modeled and the β Coriolis parameter determined based on the case

(B). The spectroscopic parameters are reported in Table 5. Taking into account the Coriolis coupling noticeably affects the B_e rotational constants of the $\Sigma_e(2_{12})$ and $\Pi_e(2_{12})$ states which change by +10.2% and −8.3%, respectively, and which are closer to each other.

4. Discussion

The present work reports high resolution IR spectroscopic jet-cooled experiments of Kr−H_2O in the region of the ν_2 band of H_2O monomer. Four *ortho* and one *para* bands have been observed and analyzed using a pseudo-diatomic model accounting for Coriolis coupling effects. The observed upper VRT states correlate to the 1_{11}, 1_{10}, and 2_{12} rotational levels of the water monomer in its $v_2 = 1$ vibrational state. The efficient rovibrational cooling ($T_R = 6$ K) of our pulsed supersonic expansion only allowed us to observe the lowest lying $\Sigma_e(1_{01})$ *ortho* state although it is only 12.192 and 21.549 cm^{-1} below the *ortho* $\Pi(1_{01})$ and $\Pi(1_{10})$ states, respectively. For the *para* spin-modification, the four lowest lying states being the $n_s = 1, \Sigma_e(0_{00})$, $\Pi(1_{11})$, $\Sigma_e(1_{11})$, and $\Sigma_e(0_{00})$ states, only the latter was observed in our experiment since it is about 30 to 40 cm^{-1} below these three other states.

Spectroscopic parameters were derived from various line positions analyses of the measurements. The band centers were found to lie within 1 cm^{-1} from those of Ar−H_2O [11, 13] implying that the energy level diagram of the complex in the $v_2 = 1$ state barely depends on the nature of the Rg atom. This result was already established for the $v_2 = 0$ state. For all 5 subbands, there is clear evidence that the upper state is perturbed. In most cases the perturbing state could be identified.

The parameters derived in this work from the analysis of the *para* $\Pi(1_{11}) \leftarrow \Sigma_e(0_{00})$ transition of Kr$-$H$_2$O, specifically the decrease of B_e with respect to B'', show that the Π_e state is Coriolis perturbed by a nearby state of the same symmetry, higher in energy. In the case of Ar$-$H$_2$O, Weida and Nesbitt [11] observed three *para* transitions, namely $\Pi(1_{11}) \leftarrow \Sigma_e(0_{00})$, $\Sigma_e(1_{11}) \leftarrow \Sigma_e(0_{00})$, and $n_s = 1, \Sigma_e(0_{00}) \leftarrow \Sigma_e(0_{00})$ which, were analyzed using a three-state model for the upper levels involving a Coriolis coupling between $\Pi(1_{11})$ and $\Sigma_e(1_{11})$ and an angular-radial coupling between $\Sigma_e(1_{11})$ and $n_s = 1, \Sigma_e(0_{00})$. Their results indicate that the angular-radial coupling strongly mixes the $\Sigma_e(1_{11})$ and $n_s = 1, \Sigma_e(0_{00})$ states. A weaker Coriolis interaction between the resulting mixed $\Sigma_e(1_{11})$ and $\Pi_e(1_{11})$ states further lifts the e/f degeneracy of $\Pi(1_{11})$ with e parity levels shifted downward and f levels upward. We can reasonably assume that a similar scenario takes place for the $\Pi(1_{11}) \leftarrow \Sigma_e(0_{00})$ transition of Kr$-$H$_2$O observed in this work, but its effects were not observed.

The *ortho* $\Pi(1_{10}) \leftarrow \Sigma_e(1_{01})$ transition of Ar$-$H$_2$O also involves coupled states for $v_2 = 1$ but the coupling between the $\Pi(1_{10})$ and $\Sigma_f(1_{10})$ states is expected to be weaker as the latter lies 15.5 cm^{-1} higher in energy. In addition to the *ortho* $\Pi(1_{10}) \leftarrow \Sigma_e(1_{01})$ transition, Weida and Nesbitt [11] observed the $\Sigma_f(1_{10}) \leftarrow \Pi(1_{01})$ *ortho* transition where the upper state is strongly coupled to $\Pi(1_{10})$. This transition could be well described by a pseudodiatomic model involving the coupled states with a fitted β off-diagonal Coriolis term within 94.8% of its theoretical value of $2B_e$. Liu and Xu [13] observed in the same region two additional transitions with upper states coupled by a Coriolis interaction, namely $n_s = 1, \Sigma_e(1_{01}) \leftarrow \Sigma_e(1_{01})$ and $n_s = 1, \Pi(1_{01}) \leftarrow \Sigma_e(1_{01})$ at 1629 and 1639.5 cm^{-1}, respectively. From a global fit of all microwave

and IR available data based on the pseudodiatomic Hamiltonian with Coriolis coupling terms mixing Σ and Π levels, they derived a fitted β value for the $n_s = 1, (1_{01})$ state within 92.4% of $2B_e$, suggesting a remaining weak coupling with a yet non-identified state. The incomplete picture of the energy scheme level of Kr$-$H$_2$O in the ν_2 region only permits to obtain a few trends provided by our rovibrational analysis: the decrease of B_f can only be explained by a Coriolis interaction with a state higher in energy, necessarily of f symmetry. More generally, the strength of the coupling can be estimated from the value of the $(B_e - B_f)/B_f$ ratio. A large value of 0.038 for the $\Pi(1_{11}) \leftarrow \Sigma_e(0_{00})$ transition is consistent with the $v_2 = 1, \Pi(1_{11})$ and $\Sigma_e(1_{11})$ being only 3 cm^{-1} apart. A smaller value of only 0.016 arises for the $\Pi(1_{10}) \leftarrow \Sigma_e(1_{01})$ transition because the $v_2 = 1, \Pi(1_{10})$ and $\Sigma_f(1_{10})$ states are 15 cm^{-1} away from each other.

The observation of both $\Sigma_e(2_{12}) \leftarrow \Sigma_e(1_{01})$ and $\Pi(2_{12}) \leftarrow \Sigma_e(1_{01})$ transitions in the present study allows us to compare the magnitude of Coriolis couplings for Ar and Kr partners and to evaluate to what extent the perturbation effects increase when going to higher energy. As suggested by previous studies [9–11], the average energy of Σ and Π states arising from the same monomer level corresponds to the energy of the unbound monomer. The energy splitting between the same Σ and Π states displays a different behavior that could be experimentally studied for Ar$-$H$_2$O [13]. In the case of the $v_2 = 1, 1_{10}$ and 2_{12} levels, an unexpected behavior is observed as it decreases from +15.5 to -5.6 cm^{-1}. In the case of Kr$-$H$_2$O, the energy splitting for the $v_2 = 1, 2_{12}$ level takes a nearly equal value of -5.3 cm^{-1}. The present investigation did not allow us to observe the $\Sigma_f(1_{10})$ state, but the values

retrieved for the rotational constants of the $\Pi(1_{10})$ state are consistent with a perturbing state higher in energy. This can be interpreted as a behavior of the Σ-Π energy splitting analogous to that of Ar$-$H$_2$O.

The Coriolis parameter β derived from the analysis of two Kr$-$H$_2$O transitions involving the coupled upper states $\Sigma_e(2_{12})$ and $\Pi(2_{12})$ is about 75% of $2B_e\sqrt{3}$, its theoretical value for $j = 2$ states [7]. This deviation of β from its theoretical values indicates that the $\Sigma_e(2_{12})$ and $\Pi(2_{12})$ states are also coupled with other states, probably higher in energy as suggested by the smaller energy difference between 2_{12} states compared to 1_{10} states. Considering the energy level diagram of *ortho* Ar$-$H$_2$O transitions in the $v_2 = 0$ state derived from far-infrared measurements [7] and the new assignments made in the present study, the most probable *ortho* state of Kr$-$H$_2$O coupled by Coriolis interactions with $\Pi(2_{12})$ is $n_s = 2, \Sigma_e(1_{01})$ at 1662.913 cm^{-1}, about 4.5 cm^{-1} higher than $\Pi(2_{12})$. In Ar$-$H$_2$O, as the Coriolis coupling constant β retrieved for the two same states accounts for only 29% of its theoretical value [13], the effects due to additional perturbing states seem more important.

Acknowledgments

PA and YB are grateful to the DIM ACAV+ Ile-de-France program for their financial support to the external cavity quantum cascade laser as part of the WATERLASER project in collaboration with LERMA laboratory.

References

[1] G. T. Fraser, F. J. Lovas, R. D. Suenram, and K. Matsumura, *J. Mol.*

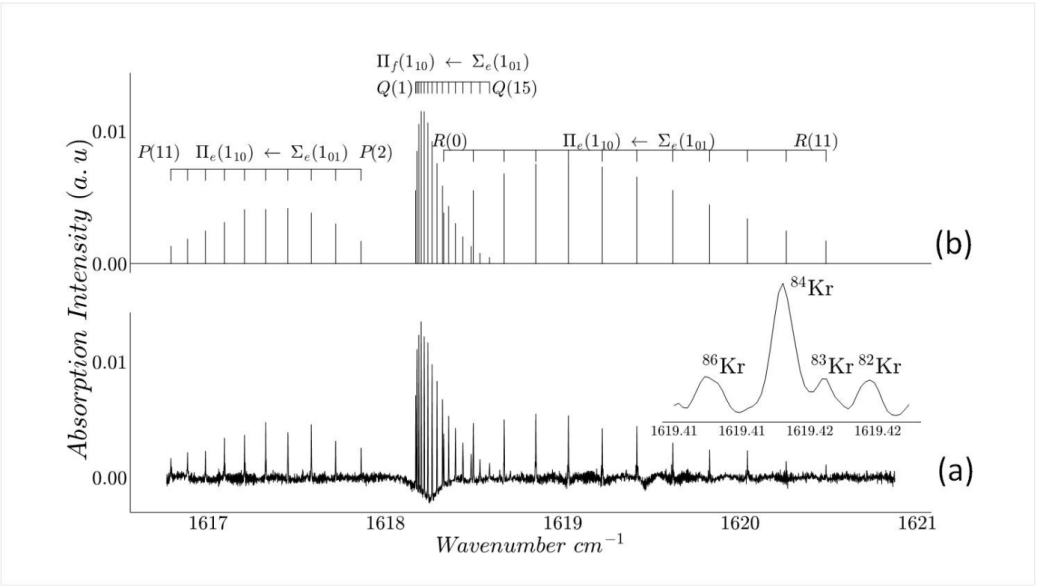

Figure 3: Jet-cooled laser spectrum of the $\Pi(1_{10}) \leftarrow \Sigma_e(1_{01})$ *ortho* transition of Kr−H_2O (a) compared to the PGOPHER fit of 33 lines using the spectroscopic parameters in Table 4. An expanded view of the $R(6)$ line of the Kr−H_2O spectrum highlights the rich isotopic structure of krypton consisting of the ^{82}Kr, ^{83}Kr, ^{84}Kr, and ^{86}Kr species.

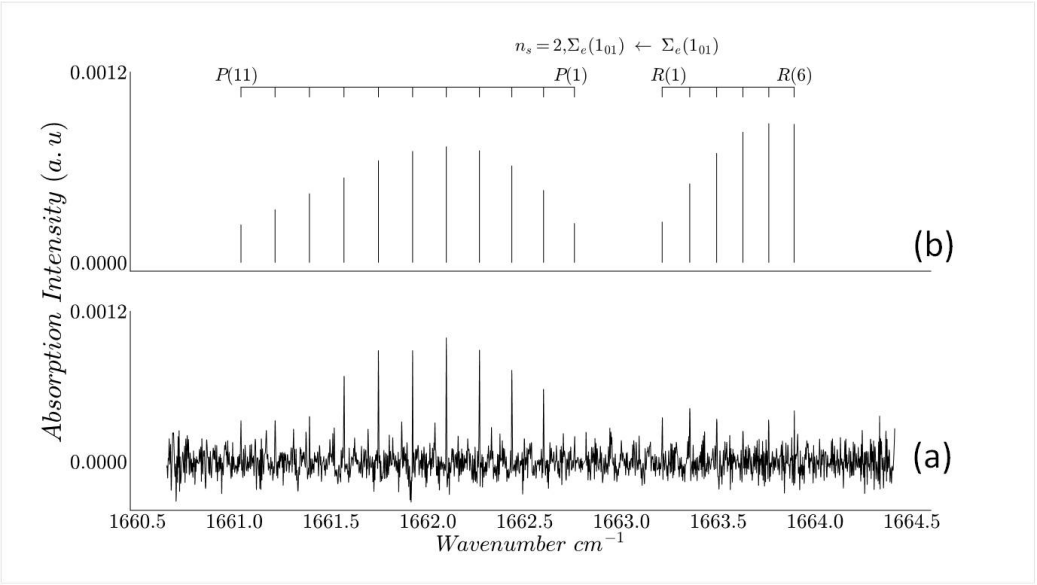

Figure 4: Jet-cooled laser spectrum of the $n_s = 2, \Sigma_e(1_{01}) \leftarrow \Sigma_e(1_{01})$ *ortho* transition of Kr−H_2O (a) compared to the PGOPHER fit using the spectroscopic parameters in Table 4.

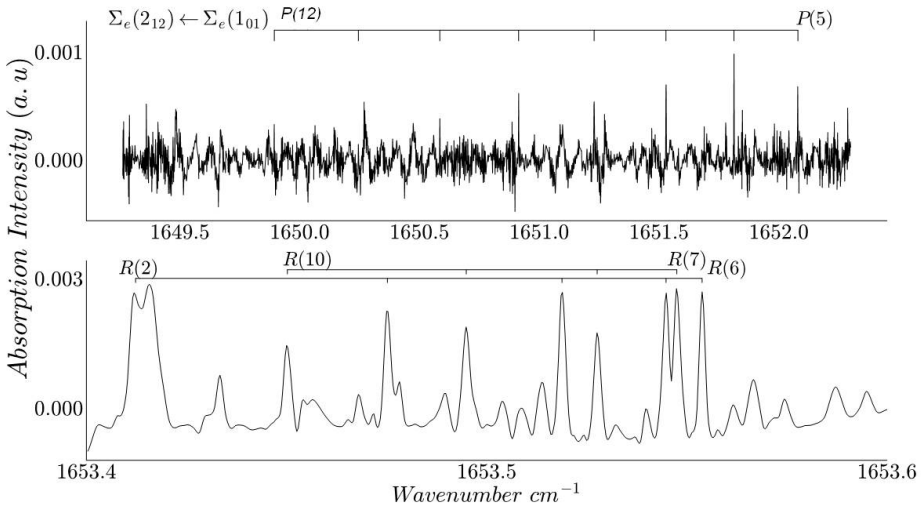

Figure 5: Jet-cooled laser spectrum of the $\Sigma_e(2_{12}) \leftarrow \Sigma_e(1_{01})$ *ortho* transition of $Kr{-}H_2O$, with a weak P branch (top) and a R branch displaying a turning point at $J = 6$ (bottom). Line assignments are reported for both branches.

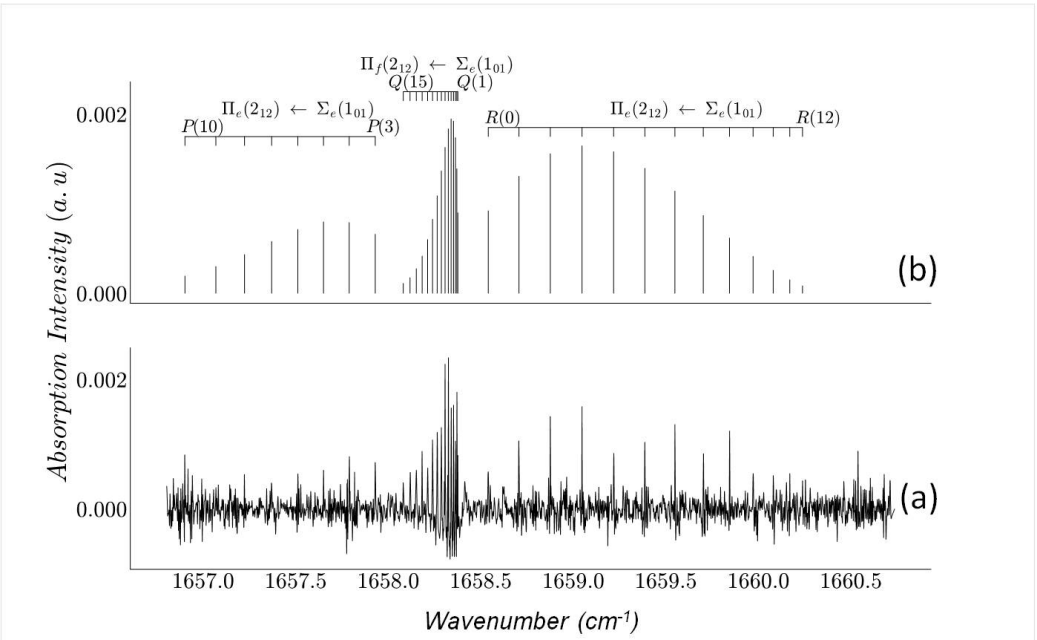

Figure 6: Jet-cooled laser spectrum of the $\Pi(2_{12}) \leftarrow \Sigma_e(1_{01})$ *ortho* transition of Kr−H_2O (a) compared to a PGOPHER stick spectrum. The Coriolis coupling of the upper states of this transition with that of the $\Sigma_e(2_{12}) \leftarrow \Sigma_e(1_{01})$ transition substantially alters the spectrum and was taken into account (b).

Table 4: Spectroscopic constants[a] from the separate analysis of the 5 transitions[b]

$v_2 = 0$	$\Sigma_e(0_{00})$		$\Sigma_e(1_{01})$		
B''	2373.1900		2327.7364		
D''	0.04899		0.03538		
$v_2 = 1$	$\Pi(1_{11})$	$\Pi(1_{10})$	$n_s = 2, \Sigma_e(1_{01})$	$\Sigma_e(2_{12})$	$\Pi(2_{12})$
ν_0	1633.7551(2)	1618.1678(1)	1662.9126(4)	1653.0870(7)	1658.3793(2)
B_e	2282.12(23)	2415.79(15)	2262.90(65)	1969.55(123)	2412.77(41)
B_f	2383.22(28)	2378.57(21)			2287.95(33)
D_e	0.0919(16)	0.0314(11)	−0.118(6)	−0.50(2)	0.796(6)
D_f	0.0643(16)	0.0296(18)			0.016(4)
$H_e(10^6)$				−944(87)	870(24)
$H_f(10^6)$					−37(11)
# lines	28	33	18	17	36
RMS	12.4	9.9	24.4	14.7	11.8

[a] Spectroscopic constants determined in the analyses reported in Sections 3.2.1 and 3.2.2 are defined in Eq. (1) and given in MHz except for band centers which are in cm^{-1}. For the $v_2 = 0$, $\Sigma_e(0_{00})$ and $\Sigma_e(1_{01})$ states, constants are from Van Wijngaarden and Jäger [27].

[b] Separate line position analyses were carried out for the $v_2 = 1 \leftarrow 0$ *para* transition $\Pi(1_{11}) \leftarrow \Sigma_e(0_{00})$ and the *ortho* transitions $\Pi(1_{10}) \leftarrow \Sigma_e(1_{01})$, $n_s = 2, \Sigma_e(1_{01}) \leftarrow \Sigma_e(1_{01})$, $\Sigma_e(2_{12}) \leftarrow \Sigma_e(1_{01})$, and $\Pi(2_{12}) \leftarrow \Sigma_e(1_{01})$.

Table 5: Spectroscopic constants[a] from the analysis of the bands[b] at 1653 and 1658 cm^{-1}

$v_2 = 1$	$\Sigma_e(2_{12})$	$\Pi(2_{12})$
ν_0	1653.0878(6)	1658.3790(2)
B_e	2170.2(622)	2212.0(625)
B_f		2288.30(3)
D_e	−0.264(27)	0.57(3)
D_f		0.019(3)
$H_e(10^6)$	−791(19)	562(39)
$H_f(10^6)$		−29(10)
β	5676(868)	
# lines	17	36
RMS	13.7	9.8

[a] Spectroscopic constants determined in one of the analysis reported in Section 3.2.2 are defined in Eqs. (1) and (2) and given in MHz except for band centers which are in cm^{-1}.

[b] Simultaneous line position analyses carried out for the *ortho* transitions $\Sigma_e(2_{12}) \leftarrow \Sigma_e(1_{01})$ and $\Pi(2_{12}) \leftarrow \Sigma_e(1_{01})$ accounting for the Coriolis coupling.

Spectrosc. **144** (1990) 97–112, doi:10.1016/0022-2852(90)90310-M.

[2] E. Zwart and W. Leo Meerts, *Chem. Phys.* **151** (1991) 407–418, doi:10.1016/0301-0104(91)80025-D.

[3] T. C. Germann and H. S. Gutowsky, *J. Chem. Phys.* **98** (1993) 5235–5238, doi:10.1063/1.464923.

[4] R. C. Cohen, Kerry L. Busarow, K. B. Laughlin, Geoffrey A. Blake, M. Havenith, Y. T. Lee, and R. J. Saykally, *J. Chem. Phys.* **89** (1988) 4494–4504, doi:10.1063/1.454789.

[5] R. C. Cohen, Kerry L. Busarow, Y. T. Lee, and R. J. Saykally, *J. Chem. Phys.* **92** (1990) 169–177, doi:10.1063/1.458459.

[6] Sakae Suzuki, R. E. Bumgarner, Paul A. Stockman, Peter G. Green, and Geoffrey A. Blake, *J. Chem. Phys.* **94** (1991) 824–825, doi:10.1063/1.460308.

[7] R. C. Cohen and R. J. Saykally, *J. Chem. Phys.* **95** (1991) 7891–7906, doi:10.1063/1.461318.

[8] Luyao Zou and Susanna L. Widicus Weaver, *J. Mol. Spectrosc.* **324** (2016) 12–19, doi:10.1016/j.jms.2016.04.010.

[9] Robert Lascola and David J. Nesbitt, *J. Chem. Phys.* **95** (1991) 7917–7932, doi:10.1063/1.461320.

[10] David J. Nesbitt and Robert Lascola, *J. Chem. Phys.* **97** (1992) 8096–8110, doi:10.1063/1.463431.

[11] Miles J. Weida and David J. Nesbitt, *J. Chem. Phys.* **106** (1997) 3078–3089, doi:10.1063/1.473051.

[12] D. Verdes and H. Linnartz, *Chem. Phys. Lett.* **355** (2002) 538–542, doi:10.1016/S0009-2614(02)00298-1.

[13] Xunchen Liu and Yunjie Xu, *J. Mol. Spectrosc.* **301** (2014) 1–8, doi:10.1016/j.jms.2014.04.005.

[14] T. Vanfleteren, T. Földes, and M. Herman, *Chem. Phys. Lett.* **627** (2015) 36–38, doi:10.1016/j.cplett.2015.03.032.

[15] Jacob T. Stewart and Benjamin J. McCall, *J. Mol. Spectrosc.* **282** (2012) 34–38, doi:10.1016/j.jms.2012.11.002.

[16] Song Li, Rui Zheng, Yu Zhu, and Chuanxi Duan, *J. Mol. Spectrosc.* **272** (2012) 27–31, doi:10.1016/j.jms.2011.12.004.

[17] K. Didriche and T. Földes, *J. Chem. Phys.* **138** (2013) 104307, doi:10.1063/1.4794161.

[18] R. C. Cohen and R. J. Saykally, *J. Phys. Chem.* **94** (1990) 7991–8000, doi:10.1021/j100383a044.

[19] R. C. Cohen and R. J. Saykally, *J. Chem. Phys.* **98** (1993) 6007–6030, doi:10.1063/1.464841.

[20] Jeremy M. Hutson, *J. Chem. Phys.* **92** (1990) 157–168, doi:10.1063/1.458485.

[21] M. Bulski, P. E. S. Wormer, and A. van der Avoird, *J. Chem. Phys.* **94** (1991) 8096–8104, doi:10.1063/1.460092.

[22] G. Chalasinski, M. M. Szczesniak, and S. Scheiner, *J. Chem. Phys.* **94** (1991) 2807–2816, doi:10.1063/1.459857.

[23] FuMing Tao and William Klemperer, *J. Chem. Phys.* **101** (1994) 1129–1145, doi:10.1063/1.468478.

[24] Matthew P. Hodges, Richard J. Wheatley, and Allan H. Harvey, *J. Chem. Phys.* **117** (2002) 7169–7179, doi:10.1063/1.1504703.

[25] Jan Makarewicz, *J. Chem. Phys.* **129** (2008) 184310, doi:10.1063/1.3009270.

[26] G. Chalasinski, M. M. Szczesniak, and S. Scheiner, *J. Chem. Phys.* **97** (1992) 8181–8187, doi:10.1063/1.463440.

[27] Jenniver van Wijngaarden and Wolfgang Jäger, *Mol. Phys.* **98** (2000) 1575–1588, doi:10.1080/00268970009483363.

[28] Qing Wen and Wolfgang Jäger, *J. Phys. Chem. A* **110** (2006) 7560–7567, doi:10.1021/jp0619890.

[29] Thomas Vanfleteren, Tomas Földes, Athéna Rizopoulos, and Michel Herman, *J. Mol. Spectrosc.* **342** (2017) 92–99, doi:10.1016/j.jms.2017.06.010.

[30] Vanfleteren, T. Földes, J. Vander Auwera, and M. Herman, *Chem. Phys. Lett.* **618** (2015) 119–122, doi:10.1016/j.cplett.2014.11.010.

[31] Pierre Asselin, Yann Berger, Thŕèse R. Huet, Laurent Margulès, Roman Motiyenko, Richard J. Hendricks, Michael R. Tarbutt, Sean K. Tokunaga, and Benoît Darquié, *Phys. Chem. Chem. Phys.* **19** (2017) 4576–4587, doi:10.1039/C6CP08724H.

[32] Y. Belkhodja, J. Loreau, A. van der Avoird, Y. Berger, and P. Asselin, *Phys. Chem. Chem. Phys.* **23** (2021) 10864–10874, doi:10.1039/D1CP00316J.

[33] M. Dehghany, Mahin Afshari, Z. Abusara, C. Van Eck, and N. Moazzen-Ahmadi, *J. Mol. Spectrosc.* **247** (2008) 123–127, doi:10.1016/j.jms.2007.11.004.

[34] Colin M. Western, PGOPHER, a program for simulating rotational, vibrational, and electronic spectra, http://pgopher.chm.bris.ac.uk.

[35] Colin M. Western and Brant E. Billinghurst, *Phys. Chem. Chem. Phys.* **21** (2019) 13986–13999, doi:10.1039/C8CP06493H.

[36] X. Liu, Thesis, University of Alberta, Department of Chemistry, Edmonton, 2013.